A Coupled Population Balance Model and CFD Approach for the Simulation of Mixing Issues in Lab-Scale and Industrial Bioreactors

Jérôme Morchain, Jean-Christophe Gabelle, and Arnaud Cockx
Université de Toulouse; INSA, UPS, INP; LISBP, 135 Avenue de Rangueil, F-31077 Toulouse, France

INRA, UMR792 Ingénierie des Systèmes Biologiques et des Procédés, F-31400 Toulouse, France

CNRS, UMR5504, F-31400 Toulouse, France

Lab-scale (70 L) and industrial scale (70 m^3) aerated fermenters are simulated using a commercial computational fluid dynamics code. The model combines an Euler-Euler approach for the two-phase flow, a population balance model for biological adaptation to concentration gradients, and a kinetic model for biological reactions. Scale-up at constant volumetric mass transfer coefficient is performed, leading to concentration gradients at the large scale. The results show that for a given concentration field and a given circulation time t_c, the population (physiological) state depends on the characteristic time of biological adaptation T_a. The population specific growth rate ($T_a \gg t_c$) is found independent of the spatial location and closely related to the volume average concentration. Oppositely, the population specific uptake rate ($T_a \sim t_c$) is spatially heterogeneous. The resulting local disequilibria between the uptake rate and the growth rate provide an explanation for the decreased performances of poorly macromixed industrial bioreactors. © 2013 American Institute of Chemical Engineers AIChE J, 60: 27–40, 2014
Keywords: computational fluid dynamics, population balance model, biokinetic model, scale-up, aerated stirred tank

Introduction

Despite the many experimental studies describing growth, production and oxygen transfer at laboratory scale, the scale-up of the process based on empirical correlations is still uncertain and many intermediate steps are necessary to progressively tune operating conditions to the desired performance. Larsson and coworkers showed that, during the scale-up of stirred tank reactors, undesired products are formed leading to a decrease in biomass yield. This problem is thought to be caused by noncontrolled pH, insufficient oxygen supply, and presence of substrate gradients, all due to insufficient mixing.[1–5] Various consequences of these heterogeneities on the microorganisms' behavior have been recently reviewed by Lara et al.[6] It has been widely demonstrated that microbial cells are affected by the fluctuations they undergo. Dunlop and coworkers pointed out the influence of intermediate mixing scales (i.e., mesomixing) on continuous cultures of *S. cerevisiae*.[7,8] The conversion yield of substrate into biomass was found to be dependent on the number and position of the injection points in a 3 L aerated bioreactor. The effects of such heterogeneities on microbial metabolism were also studied in scale-down experiments that consisted of two continuous reactors, perfectly mixed or plug flow.[1,9,10] Operating conditions of the reactors are chosen in order to expose cells to sudden variation of substrate concentration.[3,5,11–14] As a result, it has been shown that periodic exposure to excessive substrate concentration induces some modifications of the cell metabolism and leads to: (i) the over assimilation of substrates, (ii) the formation of by-products, and (iii) a decrease in the overall reactor performance.

For the prediction of gradients in a bioreactor, an alternative to the experimental approach relies on computational models that integrate both physical and biochemical phenomena.[15] In recent years, Computational Fluid Dynamics (CFD) simulation has become an effective tool to model multiphase reactors rapidly and accurately. Based on the numerical solution of the conservation equations for mass, momentum and energy, the applicability of CFD simulations has been demonstrated for single-phase and two-phase flow in various chemical engineering applications. The same approach can be successfully used for bioreactors by implementing suitable biochemical models for the reaction term. However in the very case where large concentration gradients are formed, the results are less satisfactory. Several attempts have been made to simulate a bioreactor by coupling fluid dynamics and microbial kinetics obtained from laboratory scale experiments,[16,17] using either a simplified compartment model[18,19] or a full multiphase CFD approach.[15] Very often, lower substrate consumption than expected[3] or an over-prediction of biomass yield was observed. In consequence, the parameters of the biological model (either kinetic or metabolic) had to be suited to the reactor scale. The authors of these

Correspondence concerning this article should be addressed to J. Morchain at jerome.morchain@insa-toulouse.fr.

studies agree that the key issue for successful integration of fluid dynamics and microbial kinetics is a better description of both micromixing and microbial dynamics.[15,18,20]

Our aim is to develop a consistent CFD based model for bioreactors in which the strong two-way coupling between physical and biological dynamics is accounted for. Lapin and coworkers[21,22] considered this question through a CFD Euler-Lagrange model. Here, we propose an Euler-Euler approach (for the gas-liquid flow) coupled with a population balance model for the biological phase. In two previous papers,[23,24] a single variable structured model and a population balance model dealing with the dynamic adaptation of microorganisms exposed to concentration fluctuations were developed. The main idea introduced in these papers is the "out of equilibrium" concept which states that the cell population may not be at equilibrium with its local environment. It was shown that under transient conditions, the bioreaction rates cannot be simply calculated from the local concentrations in the liquid phase. In this article, our objective is to investigate the benefits of using this concept when dealing with the scale-up of a bioreactor. Thus we consider in this study:

    i. a Euler-Euler model for the gas-liquid flow

    ii. a simple kinetic model to account for biological reactions.

    iii. a mass balance population for the dynamic adaptation to stationary concentration gradients

Two reactor scales are simulated for comparison, a pilot-size stirred tank of 70 L and an industrial-size stirred tank of 70 m³. The first part of the article is dedicated to the details of the different models used and a presentation of the scale-up strategy. Particular emphasis is placed on the analysis of the different time scales of the process and the heterogeneities induced in the gas, liquid, and biotic phases. A sensitivity analysis regarding the time scale of biological adaptation to local concentration is proposed. Owing to this approach, the formation of gradients and the resulting impact on the population of cells can be investigated. In particular, the local disequilibrium between the growth rate and the uptake rates are quantified. At the reactor scale the magnitude of the disequilibrium provides a quantitative estimate of the bioreactor efficiency. The latter is shown to be impacted by the position of the feed point.

Material and Methods

Geometry and mesh

The geometry of the tank meets the Rushton standards (see Figure 1). This geometry was already used in previous
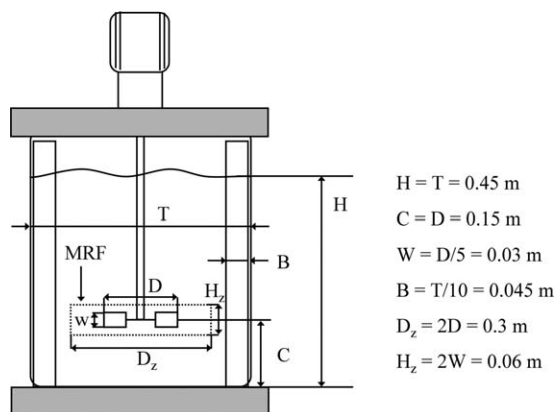

	H = T = 0.45 m
	C = D = 0.15 m
	W = D/5 = 0.03 m
	B = T/10 = 0.045 m
	$D_z = 2D = 0.3$ m
	$H_z = 2W = 0.06$ m

Figure 1. Geometry of the 70L stirred tank.

Table 1. Hydrodynamic Conditions of the Two Reactors (70 L and 70 m³)

	70 L	70 m³
Stirrer diameter (m)	0.15	1.5
Stirrer speed (rpm)	90	420
Volume (m³)	0.071	71
Specific power input (ungassed) (W/m³)	1853	1823
Gas flow rate Q_g (m³/s)	0.0008	0.08
Specific gas flow rate (vvm)	0.67	0.067
Superficial gas velocity (m/s)	0.005	0.005
Gas flow number (-)	0.034	0.016
Expected $k_l a$ (h⁻¹)	500	500

numerical[25,26] and experimental studies.[27,28] The flat-bottomed tank equipped with four flat baffles has a diameter of $T = 0.45$ m, filled with a liquid height of $H = T = 0.45$ m, corresponding to a volume of 0.07 m³. The Rushton turbine has a diameter $D = T/3 = 0.15$ m and is located at a clearance $C = D = 0.15$ m. The grid mesh was built with Gambit software and has around one million nodes. Using this mesh with the sliding mesh technique, single phase flow simulations (standard k-ε turbulence model and Large Eddy Simulation [LES]) have been extensively validated against Particle Image Velocimetry measurements.[25,26] In this work, the same grid was used but the motion of the impeller was accounted for by the moving reference frame technique (MRF). The MRF method represents a good compromise between physical and computational accuracy.[29,30] The dimension of the MRF zone is $H_Z = 0.06$ m and $D_Z = 0.3$ m. The mesh used for the simulation consisted of approximately 250,000 and 750,000 hexahedrons for the MRF zone and the stationary zone, respectively. The mean cell size in the MRF ranged from 1 mm to 3 mm. The grid of the outer zone was somewhat coarser than that of the inner zone. This grid was built for single phase flow, so the gas sparger ring was not meshed. It was modeled in a second step by a source term for the gas phase in a known volume of cells located between the bottom of the tank and the stirrer at $z = D/6$. The 70 m³ numerical model of the large scale reactor (geometry and mesh) is simply obtained by multiplying all dimensions by 10.

Operating conditions and scale-up methodology

Simulations at two scales, 70 L and 70 m³, are presented. Large-scale operating conditions are calculated following industrial rules of design. Although many scale-up rules can be applied our choice here was to keep the specific power input constant. It will be shown that this is equivalent to a scale-up that preserves the oxygen transfer capacity between the two scales. The possible oxygen depletion in bubbles at the largest sale is avoided by using oxygen enriched air in the simulations. Operating conditions for the two fermenters are reported in Table 1.

Impeller Speed and Power Consumption. For a fully turbulent one-phase system, the ungased power consumption is given by

$$P_0 = \rho_1 . N_p N^3 D^5 \tag{1}$$

In the industry, the power input ranges between 1000 and 5000 W/m³. An identical specific power input of 1800 W/m³ was chosen for both reactor sizes. Assuming a power number N_p of 5.1 for the Rushton turbine the rotational speed N of the impeller was set to 420 and 90 rpm for the 70 L and the 70 m³ tanks, respectively.

Volumetric Mass Transfer Coefficient. In aerobic processes, the volumetric mass transfer coefficient is often chosen as a scale-up criterion because it contributes significantly to the overall process performance and energy costs. Correlations for the prediction of the gas-liquid mass transfer in a stirred tank usually take the form

$$k_l a = k_l 6 \frac{\alpha_g}{d_B} \propto \left(\frac{P_g}{V}\right)^{\alpha} U_s^{\beta} \tag{2}$$

Thus, in order to maintain the oxygen transfer rate, the same specific power input and superficial gas velocity are imposed at both scales. The bubble diameter, d_B latter was assumed to be constant and was set to 1 mm. It was chosen considering the correlation of Hinze-Kolmogorov (leading to 1.8 mm in pure water) and reduced by the presence of salts in the biological medium (noncoalescing).

Gas Flow Rate and Superficial Velocity. For aerated stirred reactors, three regimes of bubbly flow: (i) flooding, (ii) loading, and (iii) complete dispersion, have been identified.[31] To maximize mass transfer, a complete dispersion of the gas phase is required. Nienow proposed that, for tanks up to 1.8 m in diameter, nondimensional boundaries of these regimes should be calculated in terms of flow number, $Fl_G = Q_g/ND^3$, Froude number, $Fr = N^2D/g$, and the geometry.[32] According to this suggestion, a constant superficial velocity, $U_s = Q_g/S_a = 0.005$ m/s, is set ensuring complete dispersion and constant gas hold-up for both scales.

Gas-liquid flow modeling

Euler-Euler Model. The commercial CFD software package Fluent® was used to solve the Eulerian balance of each phase. The k-ε model and the sliding mesh technique were chosen because of their compatibility with gas-liquid Eulerian simulation. The working fluids were water for the continuous phase ($\rho_l = 998.2$ kg/m³ and $\mu_l = 10^{-3}$ kg/m s) and air for the dispersed phase ($\rho_g = 1.2$ kg/m3 and $\mu_g = 15 \times 10^{-3}$ kg/m s). Since it is not included in Fluent®, a special "degassing" boundary condition was needed to simulate the free surface. Ranade discussed different possible approaches to treat this gas-liquid interface.[33] In our case, the free surface was modeled as a sink term for the gas phase in the layer of cells just below the liquid surface. A user defined function is developed to have a degasing condition for the bubbles and a symmetry condition for the liquid as in the work of Talvy[34,35] and Fayolle.[36] The free surface is then mobile, strengthless, and flat. The oxygen transfer from the free surface is neglected in comparison to the bubble interfacial area. This choice allows good calculation stability of the turbulent two-phase simulations with an accurate physical meaning. All other boundaries are treated as solid walls with a no-slip condition for the velocities and a standard wall treatment for the turbulent quantities.

A classical Schiller and Naumman drag law, proposed in CFD code, is used. This correlation is valid for solid spheres. In biological media, one can assume that the bubble interface is fully contaminated, so the slip velocity at the interface is null. Thus, the bubble can be considered as a rigid sphere. With this correlation, the rise velocity of a 1 mm bubble is $G = 0.113$ m s^{-1} in a stagnant fluid. Swarm effects are not considered for the gas flow rate leads to a relatively low gas hold-up (<5%). Collective effects on bubble velocity is usually neglected under 5% of gas fraction[37] but can also be neglected on mass transfer coefficient.[38] Other forces such as

lift force and added mass force are assumed to have a low impact on the gas distribution in a stirred tank. The drift effect[39] accounting for the dispersion effect due to the transport of particles by turbulent fluid motion is included.[34,35]

Scalar Transport Equation. Substrate, oxygen in the liquid, oxygen in the gas and biomass are considered as scalars. The substrate feed is modeled via a source term in the corresponding scalar transport equation. Note that the source term is zero everywhere except in the injection zone where substrate is poured at the volumetric flow rate $Q_V(S)$. Its value and that of the volume of the injection zone is such that $\rho Q_V(S).V_{inj} = Q_S$, where Q_S is the feed rate in kg h^{-1}.

Oxygen mass transfer modeling. The interfacial mass flux between the gas bubbles and the liquid N_T is expressed in terms of interfacial area, a, and transfer velocity, k_l, usually called the transfer coefficient.

$$N_T = k_l a \left(O_2^* - O_{2,l} \right) \tag{3}$$

In the case of spherical bubbles, the interfacial area is expressed as

$$a = \frac{6\alpha_g}{d_B} \tag{4}$$

The transfer coefficient k_l is estimated by the classical penetration theory of Higbie (Higbie 1935). Although more sophisticated approaches could be chosen, the local mass transfer coefficient k_l is first assumed to be constant. Its value is calculated from the expression below, using the terminal velocity of a bubble for u_R, which leads to a value of 5.36×10^{-4} m s^{-1} in the present case. A value of 5.2×10^{-4} m s^{-1} is found with the correlation of Lamont and Scott.[40] In the CFD simulation, the local relative velocity is used.

$$k_l = \frac{2}{\sqrt{\pi}} \sqrt{\frac{D_l u_R}{d_B}} \tag{5}$$

where D_l is the molecular diffusion of oxygen in pure water. The local oxygen saturation concentration O_2^* in water is estimated from Henry's law and the local concentration of oxygen in the gas $O_{2,g}$

$$O_2^* = mO_{2,g} \tag{6}$$

with m defined as follows

$$m = H_e RT \tag{7}$$

H_e is the Henry constant representing oxygen solubility in water (1.05×10^{-5} mol/m³ Pa at 25°C), R is the ideal gas constant and T is the temperature. This constant also changes with the total pressure. Taking into account enhanced solubility due to higher pressure in the bottom part of industrial reactor is often necessary. In this case, this dependency was not introduced; it will be shown that all simulations were run under oxygen nonlimiting conditions.

Biotic phase modeling

Strictly speaking, the biotic phase is a third phase in the system, but the particle Stokes number associated to the microorganisms is small enough to assume that microorganisms behave like tracers of the continuous phase.[41] Thus, the biological phase is represented here through its concentration in the liquid phase, however, it is not assumed that all individuals are identical and the concept of population balance is introduced to account for the differences between

individuals possibly induced by the concentration gradients experienced.

Population balance model. The population balance model used in this work was presented in detail in a previous paper. The main idea is that segregation among individuals is introduced based on an internal variable, e, which can be further used to compute the growth rate.[24] Owing to this approach the algebraic link between the local concentrations and the biological reaction rate is cut. This decoupling allows a true dynamic behavior to be obtained through the introduction of biological characteristic times in the model as discussed by Morchain et al.[23]

A population balance equation (PBE) describes the transport in both physical and internal variable space. A general formulation was proposed by Ramkrishna[42]

$$\frac{\partial n(\mathbf{e}, \mathbf{x}, t)}{\partial t} + u_i \frac{\partial n(\mathbf{e}, \mathbf{x}, t)}{\partial x_i} - \frac{\partial}{\partial x_i}\left(D_n \frac{\partial n(\mathbf{e}, \mathbf{x}, t)}{\partial x_i}\right) = -\frac{\partial}{\partial \mathbf{e}}(n(\mathbf{e}, t).\zeta) + h(\mathbf{e}, t) \quad (8)$$

e is the vector of internal coordinates that are used to discriminate among individuals, x is the vector of spatial coordinates, t is the time. The second and third terms on the left hand side are relative to the convective and diffusive transport in physical space. In the presence of spatial heterogeneities, these convective and diffusive terms of the general PBE will be handled by the CFD part of the model.

Thus, in the following the basic features of the model are recalled using the simplified homogeneous formulation and a single internal coordinate

$$\frac{\partial n(e)}{\partial t} = -\frac{\partial}{\partial e}[n(e).\zeta] + h \quad (9)$$

$n(e)$ represents the number of individuals in the population for which the internal property is in the range $[e, e+\Delta e]$. The variable e can be a specific rate; the specific growth rate for example or any other biological reaction rate. This is advantageous since the reaction rates are generally bounded between 0 and e_{max}, thus the PBE can be solved using the method of classes with a fixed pivot technique. Moreover, the result of the model is a distribution of biological reaction rates that can be used directly to compute the substrate production/consumption rates. The determination of the complex relationships between the cell content and the reaction rates is therefore overcome. It was shown in a previous work that a moderate number of classes such as 10 is sufficient to describe the population dynamics while limiting the computational cost.[24] The first term in the right hand side of the Eq. 9 corresponds to transport in the internal variable space. It represents the number of individuals that change in e due to favorable or unfavorable conditions in the medium (insufficient or excessive nutrient concentrations with respect to their physiological state). In this first term, ζ refers to rate of change of e with time and thus reflects the adaptation of cells.

$$\zeta = \frac{\partial e}{\partial t} \quad (10)$$

A general form for this adaptation law was proposed initially[23] and adapted to the case where e stands for the specific growth rate μ.[24] In this article, we make use of a simpler form given in Eq. 11 which preserves the main features of the adaptation law:
- the driving force of adaptation is then taken as the difference between the instantaneous value of e and the value $e*$ that would be reached in the same environment at equilibrium (for $t = \infty$). Note that we assume that the relationship between $e*$ and the concentrations in the liquid phase at equilibrium is known.
- The adaptation rate is the sum of two rates, one related to the actual growth rate μ and one independent from the cell growth ($1/T_a$).

$$\zeta = \left(\frac{1}{T_a} + \mu\right)(e* - e) \quad (11)$$

The second term on the right hand side of Eq. 9, h, represents the birth of microorganisms in a given state (value of e) due to cell multiplication.

The tunable parameter is the adaptation time constant T_a. Obviously there are numbers of biological features that adapt in response to concentration changes in the environment, so the choice of the value of T_a is not independent from the biological phenomenon associated to the variable e. For high values of T_a, adaptation is a slow process which operates at a rate comparable to the specific growth rate. This is the case for biological phenomena which are related to the cell multiplication itself; having a large characteristic time. For small values of T_a, adaptation proceeds at a rate which can be much faster than the growth rate as soon as $1/T_a \gg \mu$. Thus, the same model can be used to study the dynamic response of fast biological phenomena, with a characteristic time scale smaller than $1/\mu$. Whatever the biological rate considered, its average value is computed from the vector $\{n_i\}_e$ through the following equation

$$e^{\text{pop}} = \frac{1}{n_T} \cdot \sum_i e_i n_i \quad (12)$$

where n_i represents the number of cells for which the rate e is equal to e_i. n_T is the total cell number. The upper script pop means that averaging is performed over the population (and not spatially over the reactor).

Biological reaction model. As far as the bioreaction is addressed through a kinetic model, the internal variable e of interest is the specific growth rate μ. The same unstructured kinetic model is used for each class and the rates are dependent on the actual specific growth rate μ_i in the ith class. The number of cells in each class n_i is also replaced by the biomass concentration X_i (g/l).

The overall substrate and oxygen consumptions due to biological reactions are simply the sum of all consumptions over the classes

$$r_S = -\frac{1}{Y_{SX}} \cdot \sum_i \mu_i^a X_i \quad (13)$$

$$r_{O_2} = -\frac{1}{Y_{SX}} \frac{1}{Y_{SO}} \cdot \sum_i \mu_i^a X_i \quad (14)$$

The specific growth rate at equilibrium in a given environment is assumed to follow the Monod model with two substrates: glucose and oxygen.

Table 2. Characteristic Time Scales in the Two Bioreactors

	70 L	70 m³
Mixing time (s)	5	24
Circulation time (s)	1	5
Transfer time (s)	7.2	7.2
Substrate consumption time (s)	15	15
Growth time (s)	3600	3600
Adaptation time (growth) (s)	4000	4000
Adaptation time (uptake) (s)	40	40

$$\mu^* = \mu_{max} \frac{S}{K_S + S} \cdot \frac{O_2}{K_{O_2} + O_2} \qquad (15)$$

In Eqs. 13 and 14, μ_i^a is the minimum of μ_i and μ^*. Cells whose growth rate μ_i is greater than μ^* cannot grow at their specific growth rate because they are limited by the availability of the substrate and can only achieve μ^*. In contrast, cells whose specific growth rate is smaller than μ^* are able to grow at their own specific growth rate μ_i. More detailed explanations can be found in Ref. 24.

Problem Set Up and Resolution Strategy

Time scale analysis

The quantification of the various time scales was used to set the operating conditions; they are reported in Table 2. The mixing time scale in a turbulent stirred tank has been estimated by Nienow[31]

$$t_m = \frac{5.9}{N} \left(\frac{1}{N p_0^{1/3}} \right) \left(\frac{T}{D} \right)^2 \qquad (16)$$

Considering our scale-up procedure (same volumetric power draw), the impeller rotation speed N is smaller at the large scale than at the small scale. This led to a mixing time five times longer. A more relevant time scale to consider here is the circulation time which is a fraction (1/5) of the mixing time.

The characteristic time associated with oxygen mass transfer, t_{tr}, is taken as the inverse of $k_L a$.[6] The time scale of the substrate assimilation, t_S, is determined from the volumetric average concentrations (noted $< >$) as

$$t_S = \frac{\langle S \rangle}{\mu_{max} Y_{SX} \cdot \langle X \rangle} \qquad (17)$$

The time scale associated with the biomass growth, t_X, is taken as the inverse of μ_{max}.

The last time scale to consider is the time scale of biological adaptation, T_a. This time scale defines how fast the population adapts in response to a change in the concentrations. Two values will be considered: one large compared to the circulation time and the other similar to the circulation time.

It is important to observe that the time scale for growth and that for substrate consumption are different, the latter being dependent on the amount of microorganisms. Thus, it decreases during the course of a fed-batch fermentation. In that sense, aiming at maximum productivity always pushes the fermentation towards a more severe competition between mixing and reaction. Since the time scale for growth is much larger than all the other time scales, it is reasonable to neglect cell multiplication and perform simulations with a constant biomass concentration. Considering cell multiplication would require in a continuous change in the feed rate

further leading to continuous changes in the concentration gradients and in the concentration of biomass. Inversely, keeping the biomass concentration constant allow the examination of the sole effect of the adaptation dynamics on the heterogeneity of the biological phase in a stationary concentration field. Anyway, considering cell multiplication is possible in the modeling approach proposed as shown in a previous paper.[24]

Operating conditions

The same average concentrations (for substrate and biomass) were used at both scales. These concentrations were chosen so that mixing is faster than reaction at the small scale and competes with reaction at the large scale. The biomass concentration is constant and set to $X = 10$ g L^{-1}. The results presented thus correspond to a snapshot of a fed-batch culture when $X(t) = 10$ g L^{-1} or a continuous culture at the same biomass concentration.

The last parameter required for the simulation is the substrate feed rate. From a mass balance on the substrate in the reactor under the assumptions of perfect mixing, homogeneous hold-up and no oxygen limitation, one can calculate an estimation of the specific growth rate noted μ_∞. This variable is further referred as a macroscopic specific growth rate since it is based on a mass balance at the macroscopic scale of the reactor.

$$Q_S = Y_{SX} \mu_\infty \langle X \rangle \left(1 - \langle \alpha_g \rangle \right) . V \Rightarrow \mu_\infty \cong \frac{Q_S}{Y_{SX} \left(1 - \langle \alpha_g \rangle \right) \langle X \rangle V} \qquad (18)$$

In order to produce large-scale gradients, the substrate concentration was chosen to be low on average and the value of Q_S was set according to the previous equation in order to reach a ratio μ/μ_{max} roughly equal to 0.5, that is, $<S> \cong K_S$. The inlet oxygen concentration in the gas phase was chosen in order to avoid limitations, set to 800 and 900 mg L^{-1} for the 70 L and 70 m³ reactors, respectively. As a result of our choices, the 70 L reactor is expected to be homogeneous (since $t_m \ll t_s$) whereas substrate concentration gradients should appear in the large scale reactor (for $t_m > t_s$). Simulations at two different scales thus only differ by the size of the reactor. In any situation, growth is not taken into account because the time scale for growth is much longer than the others. At the large scale, two injection point locations will be considered: one at the top of the reactor and one near the impeller.

Solution strategy

Single phase simulations are first run in steady mode. Then the injection of gas is added to the model and the Euler-Euler simulations are performed. The converged velocity and turbulence fields previously calculated are used as initial conditions. The 3D bubbly flow in a stirred tank is

Table 3. Parameters for the Comparison with Bombac's Experiments

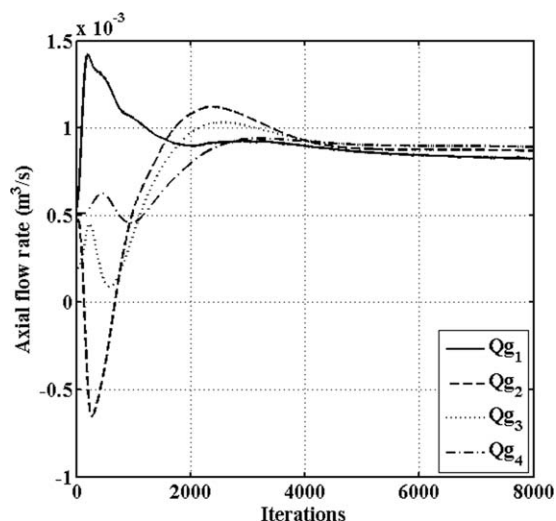|	70 L	70 m³	Figure 5a	Figure 5b	Figure 5c
D (m)	0.15	1.5	0.15	0.15	0.15
Q_g (m³ s^{-1})	0.0008	0.08	0.0006	0.0017	0.0017
N (s^{-1})	7	1.5	6.27	6.27	6.27
Fl$_G$ (-)	0.034	0.016	0.026	0.079	0.112
Fr (-)	0.75	0.34	0.6	0.6	0.3

Figure 2. Vertical gas flow rate at different heights (z = 0.1 m, z = 0.25 m, z = 0.35 m and z = 0.44 m) in the 70L reactor.

mostly unstable, especially, at the large scale because density-gradient-induced flow patterns are present.[43] Therefore, convergence of steady state simulations is difficult to achieve. Two phase flow simulations without reaction were conducted in the unsteady mode. The simulations were run in double precision with the segregated implicit solver. The temporal discretization scheme was 1st order implicit. Beyond numerical convergence based on residuals ($<10^{-5}$), three different physical convergence criteria were chosen to assess the accuracy of the solution: a constant torque on the impeller, a constant mean gas hold-up and a constant vertical gas flow rate through a series of cross sections located at different heights. As shown in Figure 2, simulations were run until an identical value is found in each section. Once the turbulent two-phase flow is obtained, the velocities (in both phases), turbulence and volume fraction fields are frozen. PBEs for microbial adaptation dynamics and those for the scalar concentrations are incorporated in the model. Glucose
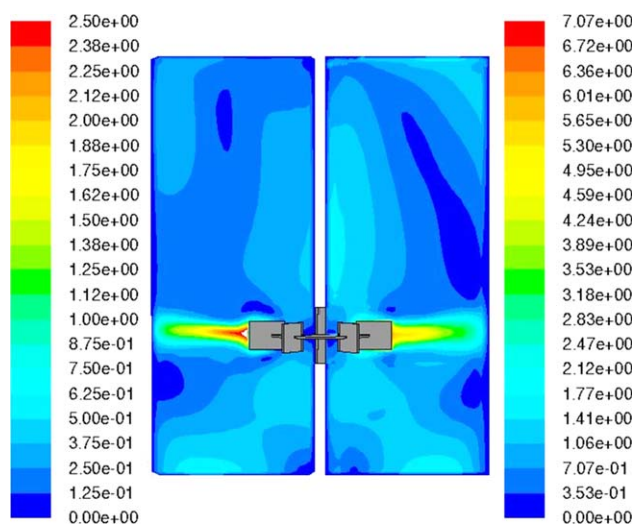
feed, oxygen mass transfer, glucose and oxygen consumptions due to biological reactions are now considered: two-phase mass transfer, scalar transport, biological reactions, and biological adaptation are treated altogether. In this context, the interactions between mixing, transfer, and reaction will determine the results. Initially, cells are homogeneously distributed in the 10 classes of the population balance model. Steady state simulations are run until numerical and physical convergence criteria are satisfied. The latter will be presented in detail in the next section. Source and sink terms for substrate, oxygen and biomass concentration as well as mass transfer terms were added to the CFD code through Used Defined Functions.

In this work two asymptotic cases (slow adaptation and fast adaptation) are studied. This was done consecutively as explained hereafter. To begin with, the population balance model is run with e corresponding to the specific growth rate. Once a steady state is reached, a vector $\{X_i\}_\mu$ as well as the concentration fields of all substrates in the gas and liquid phases are obtained. The vector $\{X_i\}_\mu$ defines the local value of the population specific growth rate μ^{pop}. A full two-way coupling for a slow biological phenomenon is thus completed. Then, the corresponding substrate and oxygen concentrations fields are frozen and a fast responding population is transported in that heterogeneous concentration field. This allows the examination of the consequences of a realistic heterogeneous concentration field on the production of heterogeneities within a population of cells (whom growth rate is known) when the characteristic time of the biological adaptation is small.

Results

Hydrodynamics

As already mentioned, an intensive validation of the numerical results and an assessment of Reynolds Averaged Navier-Stokes equation (RANS) vs. LES simulations have been previously published.[25] The contours of velocity magnitude plotted on a vertical plane are reported in Figure 3, for the 70 L (left) and the 70 m^3 (right) reactors, respectively. Note that the color ranges are different. The simulated flow fields appear to be in reasonable agreement with expectations.[30] At both scales, recirculation loops are observed above and below the stirrer. The reactor is divided into two zones by the jet stream generated by the Rushton turbine. Because of geometry scale-up at the same specific power input velocity maps are very similar.

In the case of aerated systems, the power consumption is lower than in unaerated systems (P_0) due to the presence of cavities behind the blades.[44] In our simulations, the gassed power consumption (P_g) can be calculated from post processing the torque on the stirrer. The results, reported in Table 4, show that the relative power demand (P_g/P_0) for the

Figure 3. Contours of velocity magnitude (in m.s^{-1}) in a vertical plane (left 70 L, right 70 m^3).

Note the different scale for each side. [Color figure can be viewed in the online issue, which is available at wileyonlinelibrary.com.]

Table 4. Power Draw and Gas Hold-Up

	70L	70 m^3 Top Feed	70 m^3 Bottom Feed
P_g/P_0			
Numerical simulation	0.6	0.96	0.96
Estimated	0.59[a]	0.83[a]	0.83[a]
Gas hold-up ε_G [%]			
Numerical simulation	4.9	4.7	4.7
Gabelle (2012), see eq. 19	4.67	4.67	4.67
Homogeneous regime, see eq. 20	4.5	4.5	4.5

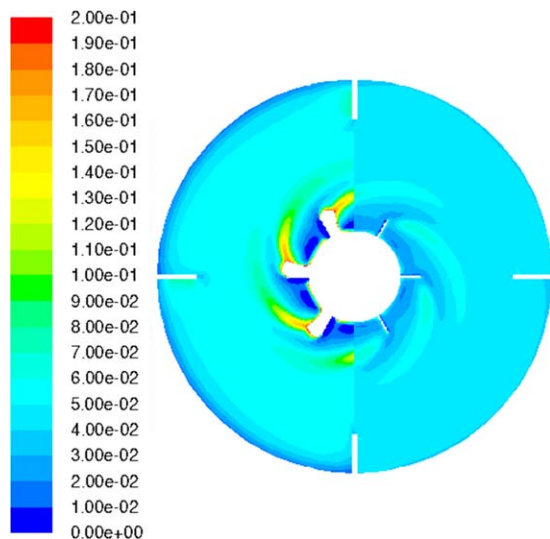[a]Calculated by the correlation of Gabelle et al.[45]

Figure 4. Gas hold-up distributions in the plane of the stirrer (left 70 L, right 70 m³).

The same colour scale applies for both sides. [Color figure can be viewed in the online issue, which is available at wileyonlinelibrary.com.]

70-L reactor is equal to 0.6 which closely matches the value calculated by the correlation recently published by Gabelle et al.[45] For the industrial scale, the ratio P_g/P_0 calculated by the software is slightly higher than that predicted by the correlation. We also note that, in the work of Delafosse,[25,26] at pilot scale and without gas, the numerical value for the torque is in very good accordance with the theoretical value. These results prove that the mesh is suitable for both scales and that the local shear stress around the impeller is accurately calculated in a two-phase system also.

A mass balance in homogeneous regime gives an estimate of the average gas-hold up, $<\alpha_g>$, by dividing the gas flow rate by the gas slip velocity G times the cross section, S. A value of 4.5% is found with this method.

$$\langle \alpha_g \rangle = \frac{Q_g}{SG} \qquad (19)$$

In Table 4, gas hold-up predicted by the simulation is compared with values calculated through the expression above under the assumption that bubbles rise at $G = 0.113$ m s^{-1} (terminal rise velocity calculated by Schiller and Naumman's correlation for the drag coefficient). The results are also in good agreement with the expected gas hold-up and also compare favorably with the correlation of Whitton and Nienow[46] and the following correlation of Gabelle[47]

$$\langle \alpha_g \rangle = 6 \left(\frac{P_g}{V} \right)^{0.32} \left(\frac{Q_g}{S} \right)^{0.49} \qquad (20)$$

At small scale, the mean gas hold-up is slightly higher than expected because of gas accumulation behind the blades. As shown in Figure 4, at small scale, some cavities marked by a gas fraction above 20% appear behind the blades. Such cavities can be observed in real systems according to Bombac et al.[48] and Scargiali et al.[30] Bubbles are attracted in low pressure zones. In the simulations, a high value of gas fraction is calculated in a small volume behind the blades. This phenomenon is not fully representative of a real system because, at that gas fraction level, coalescence is believed to occur and then the bubble slip velocity should increase. As we have considered a constant bubble diameter in an Eulerian approach, the model presented in this article cannot describe the presence of large cavities behind the blades accurately.

In Figure 5, three experiments of Bombac et al. are reported. The vessel height and diameter are the same as those of our 70 L fermentor. The stirrer is placed at one-fourth of the vessel diameter while, in our simulation, it is located at one-third (standard reactor). Each experiment corresponds to one type of structure (Vortex-Clinging structure,
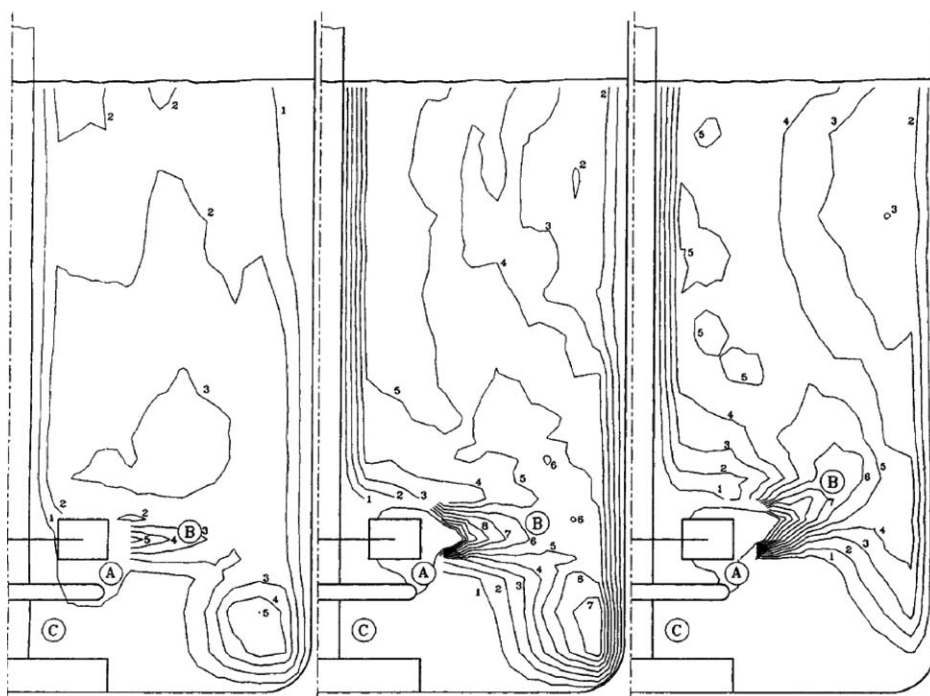

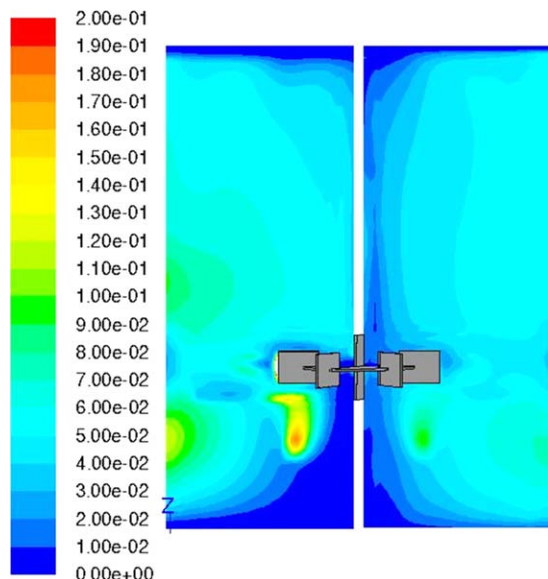**Figure 5. Gas-hold-up distributions from Bombac et al.[46]**

Figure 6. Gas hold-up distributions in a vertical plane (left 70 L, right 70 m³).

The same colour scale applies for both sides. [Color figure can be viewed in the online issue, which is available at wileyonlinelibrary.com.]

small "3-3" structure (S33) or large "3-3" structures (L33)). Operating conditions are reported in Table 3. Using a ratio of one-fourth of the vessel diameter (instead of one third), Bombac showed that the ungassed zone below the impeller was reduced remarkably in all hydrodynamic regimes. Then, in fully established recirculation, all measured structures were detected at lower flow numbers than those predicted by correlations found in the literature. Bearing this in mind, our CFD simulations (Figure 6) are qualitatively in good agreement with Bombac's experiments examined in terms of gas hold-up contours and cavity structures. Figure 6 also shows that the large-scale reactor is more homogeneous in terms of gas hold-up than the small one. In the latter case, the gas hold-up below the impeller is indeed higher than the average

value. This can be explained by the presence of a loop in the sparger zone where bubbles can be trapped.

Reacting species: Two-way coupled simulations

Slow biological process. This part focuses on the results obtained with a population balance model using the specific growth rate as the discriminating parameter between individuals (e≡μ_i in Eq. 11). The characteristic time T_a associated to the specific growth rate adaptation is long compared to the mixing time; specific growth rate adaptation is a slow process. For each class in the PBM, the driving force of adaptation is the difference between the specific growth rate at equilibrium μ^* (based on the concentrations in the liquid phase) and the specific growth rate μ_i of that class. The results are presented in Table 5. All the mass balances are accurately satisfied since relative errors are very small. At large scale with top feed injection, the difference between the oxygen consumption and the oxygen transfer is well balanced (around 4.58%). The overall substrate consumption rate also closely matches the feed rate (0.16%). Note that the oxygen concentration is everywhere much larger than K_{O_2} (0.1 mg L^{-1}) and it has therefore almost no impact on the calculation of the local specific growth rates. On the contrary, the sugar concentration field is spatially heterogeneous.

The difference between $\Gamma(<S>)$ and $<\Gamma(S)>$ is first used to identify the presence of concentration gradients in the reactor. The Γ function defined in Table 5. It can be seen that perfect homogeneity is obtained at the small scale whereas some heterogeneities exist at the large scale. It could be thought that the difference as small as 4×10^{-3} between $\Gamma(<S>)$ and $<\Gamma(S)>$ is within the numerical uncertainty but it is not (in fact a difference of 10^{-6} is reached in the 70L bioreactor). However, the hyperbolic form of the Γ function and the volume integration dampen the effects of gradients. Another way to inspect the concentration gradients is to look at the substrate volume distributions. These are plotted in Figure 7 for the top feed point and the bottom feed point. Since the average sugar concentration is different in each case, the centered variable S-<S> is considered. The difference between the two reactor designs lies in the presence of relatively higher sugar

Table 5. Numerical Simulation Results for the Lab-Scale and Industrial Scale Bioreactors

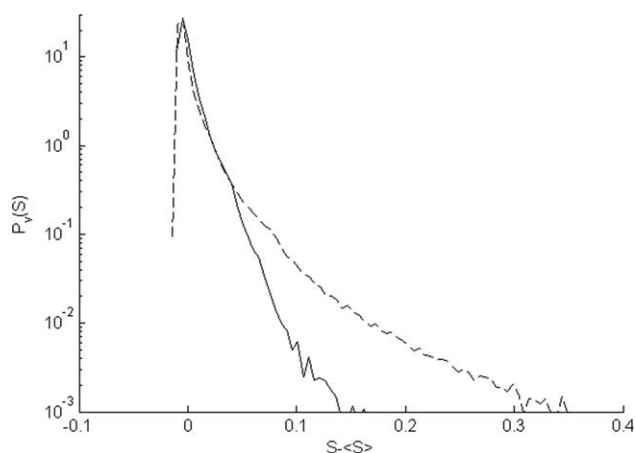|		70 m3	
	70 L	Top Feed	Bottom Feed
Q_S (kg h^{-1})	0.319	355.4	318.9
$R(S) = \iiint\limits_V r_S dv$ (kg h^{-1})	0.324	354.8	318.5
$T(O_2)$ (see Appendix) (kg h^{-1})	0.325	338.5	312.8
$(R(S)-T(O_2))/R(S)$ (%)	−0.11	4.58	1.80
$(Q_S-R(S))/Q_S$ (%)	−1.41	0.16	0.10
$<S>$ (mg L^{-1})	48.4	67.8	53.0
$<O_{2,liq}>$ (mg L^{-1})	14.5	3.55	3.52
$<O_{2,gas}>$ (mg L^{-1})	799	438	413
$\Gamma(<S>) = <S>/K_S+<S>$	0.492	0.569	0.514
$<\Gamma(S)> = <S/K_S+S>$	0.492	0.575	0.510
$\Gamma(<O_{2,liq}>) = <O_{2,liq}>/K_{O2}+<O_{2,liq}>$	0.993	0.972	0.972
$<\Gamma(O_{2,liq})> = <O_{2,liq}/K_{O2}+O_{2,liq}>$	0.993	0.973	0.972
μ_∞/μ_{max}	0.480	0.527	0.472
$\mu/\mu_{max} = f(<S>,<O_{2,liq}>)$	0.488	0.560	0.500
$<\mu^*>/\mu_{max} = <f(S,O_{2,liq})>$	0.488	0.553	0.496
$<\mu^{pop}>/\mu_{max}$	0.487	0.526	0.472

Figure 7. Volume distributions of the centred substrate concentration S-<S> in the 70 m³ bioreactors.

Continuous line: bottom feed point. Dashed line: top feed point

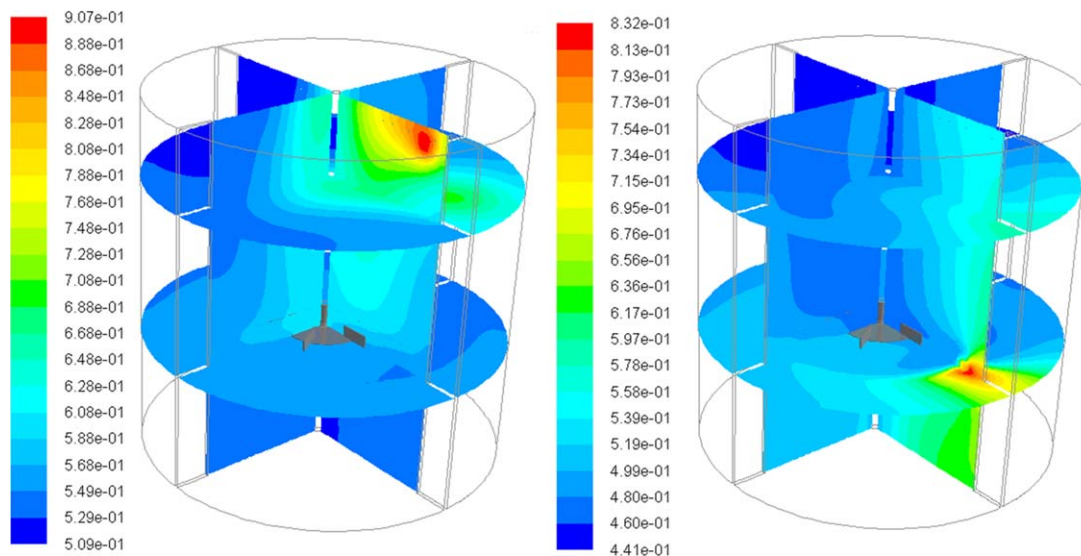**Figure 8. Contours of μ^*/μ_{max} in the 70 m^3 bioreactor.**

Top feed (left). Bottom feed (right). [Color figure can be viewed in the online issue, which is available at wileyonlinelibrary.com.]

concentration with the top feed injection. This can only be appreciated using logarithmic coordinates for the *y*-axis because the zone of elevated concentrations only represents a small fraction of the total volume. As expected, better homogenization is achieved if the substrate is fed in the discharge of the impeller where the local energy dissipation is more important.[49] Accordingly, the variance of the centered concentration distribution is 0.04 for a feed point located in the discharge of the impeller, whereas it goes up to 0.11 with a feed point in the upper part of the reactor. Thus, the volume distributions $p_V(S-<S>)$ clearly indicate that positioning the feed point near the impeller reduces the substrate gradients in the bioreactor. This design should therefore represent a better option if cells are highly sensitive to concentration fluctuations.

The impact of substrate gradients can be appreciated in Figure 8 where the contours of the ratios μ^*/μ_{max} are plotted on two vertical and one horizontal planes. The concentration gradients induce spatial variations of the local equilibrium specific growth rate μ^*. Near the injection point, the local specific growth rate ($\mu^*/\mu_{max} = 0.9$ for the top feed, $\mu^*/\mu_{max} = 0.83$ for the bottom feed) is almost twice the average

value in the reactor ($<\mu^*>/\mu_{max} = 0.5$). However the field of μ^* constitutes a static vision for these graphs show the local values of the specific growth rate that could be reached owing to the local concentrations if the residence time of the microorganism at each location was infinitely long. Should these local values of μ^* be used to calculate the bioreaction rates, one would assume that cells are instantaneously at equilibrium with their environment: adapted and able to grow at the rate defined by the local concentrations. A more realistic vision must include the dynamics of both the flow and the biological adaptation.

In our dynamic modeling approach, a time constant $T_a \sim 1/\mu_{max} = 4000$ s for the specific growth rate adaptation to the local concentration was introduced. The resulting population state vector is the same in each zone of the reactor: the normalized volume distributions p_V are delta functions ($\delta(X_i-<X_i>)$) as it can be seen in Figure 9a. Whatever the elementary volume picked in the reactor, $X_i=<X_i>$ and the sum of all the elementary volume where $X_i = <X_i>$ equals the total volume of the reactor ($p_V = 1$). Thus, the spatial heterogeneities of the substrate concentration fields result in no heterogeneity in the population specific growth rate.
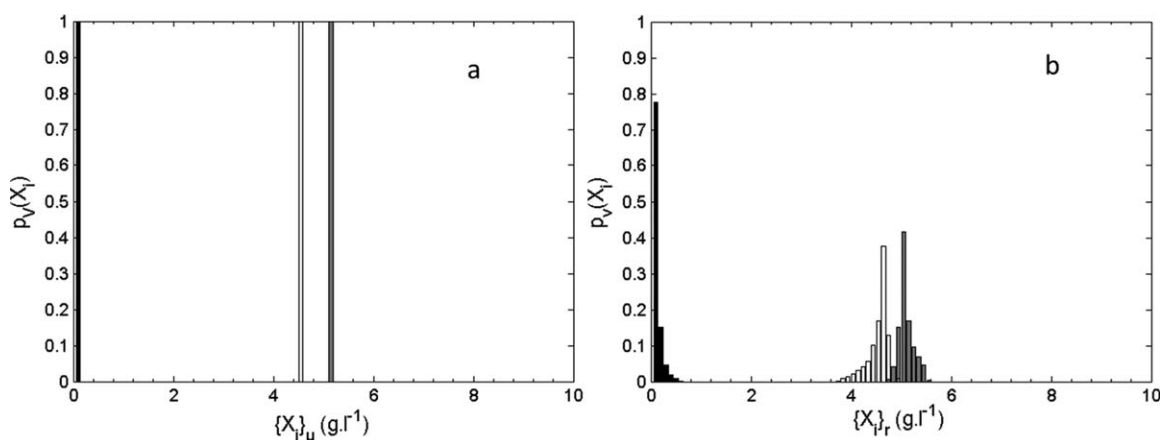

Figure 9. Normalized volume distributions of X$_4$ (white), X$_5$ (grey) and X$_6$ (black) in the 70 m^3 bioreactor with top feed point: (a) growth rate, (b) uptake rate.
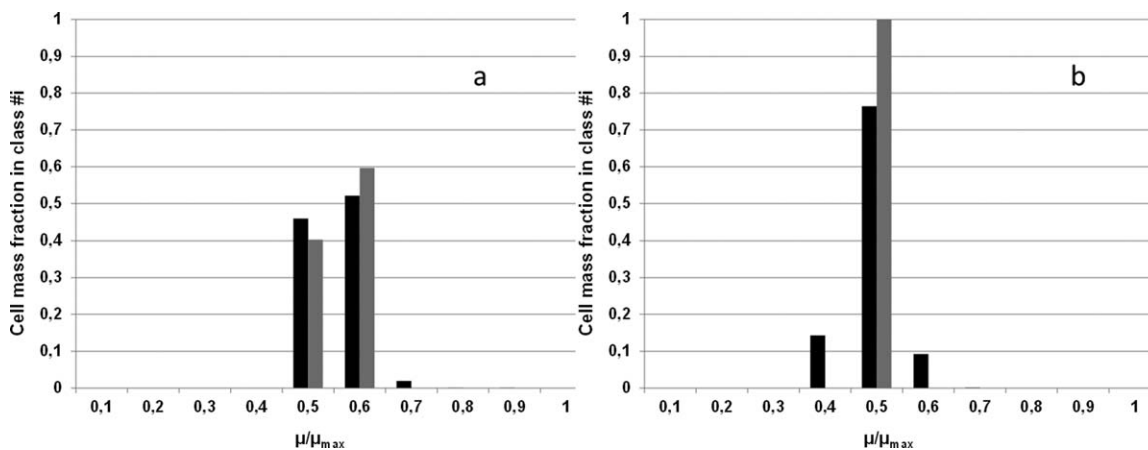
Figure 10. Normalized distribution of the cell population in the μ-space in the 70 m³ bioreactors.
CFD simulated distribution at the large scale: black. Theoretical distributions based on perfectly mixed hypothesis: grey.

The spatial variations of the local specific growth rate μ^* are actually filtered by the population of microorganisms since the characteristic time of the specific growth rate adaptation T_a is much larger than the circulation time (comparable to the mixing time in Table 2). In other words, cell will visit the entire reactor by the time they adapt and the resulting population specific growth rate is the integrated consequence of all the concentration along the trajectories[5] (concentration value and time exposure to the latter).

Now one can examine the population specific growth rate distribution. Figure 10 shows this normalized distribution X_i/X_T as a function of the ratio μ/μ_{max} in the 70 m³ bioreactors with top feed (a) and bottom feed (b) injection. The CFD based distributions in the heterogeneous bioreactors are colored in black. The total population is distributed in the μ-space and the resulting vector $\{X_i\}_\mu$ allow the calculation of μ^{pop}

$$\mu^{pop} = \frac{1}{X_T} \cdot \sum_i \mu_i X_i \qquad (21)$$

The grey bars correspond to the distributions that would be obtained in a homogeneous reactor with the same S and O₂ average concentrations. In the 70 m³ bioreactor with bottom feed, the ratio $\mu/\mu_{max} = f(\langle S \rangle, \langle O_{2,liq} \rangle) = 0.5$ (see Table 5). In the homogeneous case, the whole population would lie in the 5th class (see Figure 10b). Under the same hypothesis, in the 70 m³ bioreactor with top feed, the ratio $\mu/\mu_{max} = f(\langle S \rangle, \langle O_{2,liq} \rangle)$ would be 0.56 and the population be distributed in the two classes surrounding this value: 40% in class #5 ($\mu/\mu_{max} = 0.5$) and 60% in class #6 ($\mu/\mu_{max} = 0.6$) (see Figure 10a). The actual distributions (in black) reflect the combined effects of substrate concentration fields and local residence times on the production of heterogeneity within the population. One concludes that if the time constant of biological adaptation is much larger than the circulation time, the population averaged specific rate of the corresponding biological process is independent of the spatial location. However, a distribution of the specific rates exists within the population.

Fast biological process. Now let us consider a biological process with a characteristic time comparable to the circulation time, say 40 s in the 70 m³ reactor. In order to study this situation, the population model is run with $T_a = 40$ s and the variable e now stands for the specific rate (e≡r$_i$ in Eq.

11) of another biological phenomenon. An example of such a phenomenon is the dynamics of the substrate uptake.[50] Thus, the vector $\{X_i\}_r$ is now used to compute the local value of the population specific uptake rate, r^{pop}. It is still assumed that the uptake rate at equilibrium is related to the substrate concentration in the liquid phase through an algebraic equation such as Eq. 15, that is, $r^* = f(S)$. Since the characteristic time is similar to the circulation time, stronger interaction exists between the substrate concentration distribution and the local values of the specific uptake rate. However, the dynamics of the uptake system is not infinitely fast. As a consequence, the uptake rate at a given location cannot be deduced from the local concentrations only. Here again, it results from the dynamic interaction between the concentration field, the local residence time and the dynamics of the uptake system itself. It is illustrated in Figure 9b where the volume distribution of the components of vector $\{X_i\}_r$ differ from delta functions. This means that the population uptake rate is now dependent on the location. Thus, if the time constant of biological adaptation is similar to the mixing time, the population state is different in each zone of the reactor. The gradient of substrate in the liquid phase results in significant heterogeneities in the biological population.

Discussion

Using a biological dynamic model with a large time constant, we found that the population specific growth rate (computed from $\{X_i\}_\mu$) is different from the local equilibrium values μ^*. This is a very important feature of this dynamic modeling approach. Indeed, if one calculates the specific growth rate as the local growth rate μ^*, one actually assumes that the population instantaneously adapts its behavior to the local concentrations. This unjustified assumption is generally made in the CFD simulation of bioreactors. On the contrary, our dynamic approach predicts that the population specific growth rate μ^{pop} can be different from the local growth rate μ^*, that is, decoupled from the local concentrations as observed in many experimental situations.[12,51,52] It can be seen in Table 5 that $\langle \mu^{pop} \rangle$, μ and $\langle \mu^* \rangle$ differ at the large scale whereas they are identical in the lab-scale homogeneous bioreactor. It is observed that

i. The overall substrate consumption exactly matches the amount of substrate poured into the reactor. Only in this situation it is possible to estimate the average
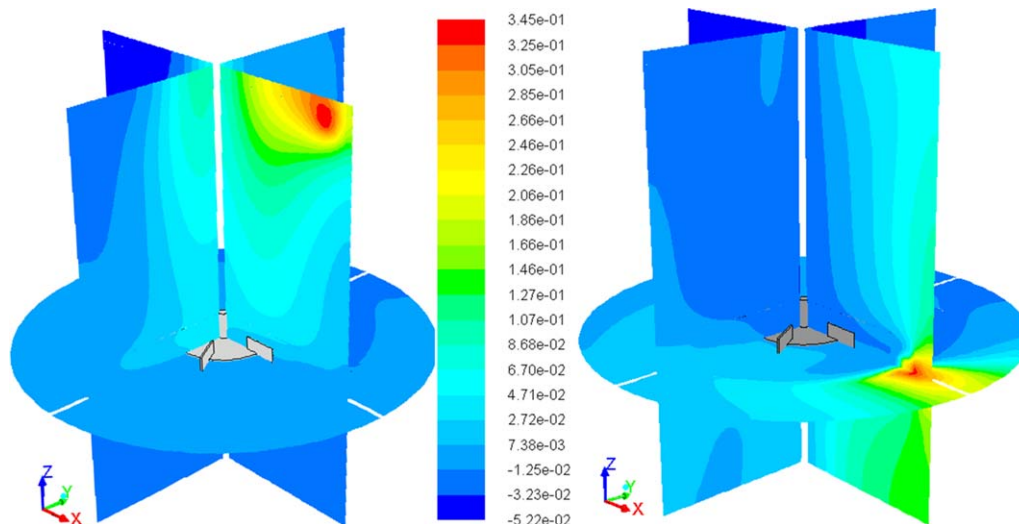
Figure 11. Contours of the difference μ^*-μ^{pop}: specific growth rate computed from the local concentrations minus population specific growth rate.

Top feed (left). Bottom feed (right). [Color figure can be viewed in the online issue, which is available at wileyonlinelibrary.com.]

growth rate of the population $<\mu^{pop}>$ from a mass balance on the entire reactor (Eq. 18)

ii. $<\mu^{pop}>$ is smaller than μ^*: for a given heterogeneous concentration field, the real population growth rate is always smaller than the value obtained assuming local equilibrium. This equilibrium value can only be reached in a perfectly mixed reactor.

The differences increase with the heterogeneity of the concentration field. These results show that the population specific growth rate cannot be accurately calculated from the volume average concentrations or by averaging the local growth rates. These two approaches would overestimate the actual specific growth rate. Nevertheless, if need be, these constitute a fairly good approximation (error < 5%).

Although the consequences on average are very small, $<\mu^*>$ and $<\mu^{pop}>$ are very similar and only discernible numerically, it is remarkable to observe that the discrepancies between μ^{pop} and μ^* can be locally significant. Even if the local differences between equilibrium value and population growth rate can be positive or negative, the average specific growth rate value on the whole reactor is systematically lower than equilibrium value. The contours of the difference between these two quantities, μ^*- μ^{pop}, are presented in Figure 11. The same color map is used for the two bioreactor designs, so it is clearly visible that, from the microorganisms' point of view, the reactor on the left (top feed injection point) is much more heterogeneous than the reactor on the right. Positive and negative difference zones are discernible. In a perfectly mixed reactor, the difference would be null everywhere.

Negative values indicate that a fraction of the population is facing a suboptimal environment. In these zones, the growth capacity of some cells is not fully exploited because the local concentrations are limiting. On the contrary, positive values indicate that the population is growing at a specific rate which is lower than the value that could be reached at equilibrium owing to the local concentrations. This suggests that the population is exposed to an excess of nutrient with respect to its own needs (for growth). The interesting point is that the local concentrations are not necessarily limiting concentrations in the classical sense. In our approach,

the concept of limitation (or excess) now becomes relative to the population state, related to the difference μ^*-μ^{pop}. It can be a good objective from an industrial point of view to minimize this difference in large scale bioreactors. Note that it increases with the biomass concentration and decreases with the agitation speed.

A further step in the analysis of the results is proposed through the examination of the difference between the population uptake rate and the population growth rate. Indeed, it was shown that under limiting conditions ($S<K_S$ in this case), the uptake rate is decoupled from the growth rate.[51,53,54] This is particularly the case when microorganisms are repeatedly exposed to high and low substrate concentrations, as it is the case here in a heterogeneous bioreactor. At equilibrium, these two rates are equal: the uptake rate matches the cell needs. A difference between the two indicates that the microorganisms are "out of equilibrium." The contours of the difference r^{pop}-μ^{pop} are presented in Figure 12. In this figure μ^{pop} is computed from the stored vectors $\{X_i\}_\mu$ obtained in the previous simulations (with a large value for T_a). Note that the difference r^{pop}-μ^{pop} is non-zero because the two biological phenomena obey different dynamics.

On the one hand, in zones where r^{pop}-μ^{pop} is positive, the amount of sugar assimilated exceeds the cells' needs for growth. This extra assimilation might lead to overflow metabolism and by-products formation. On the other hand, in zones where the difference is negative, the substrate demand for growth is not satisfied and alternative carbon sources may be used to complement the cell needs. These could correspond to by-products reassimilation zones.[5] Assuming that the perturbation on cell metabolism is related to the maximum value of the difference r^{pop}-μ^{pop} and observing that this difference is larger for the top feed injection, one can presume that bottom injection is less detrimental to the cells. So it is found that the feed point location may have an effect on the population behavior whilst leaving the overall uptake rate unchanged as experimentally observed by Namdev et al.[55]

To conclude it is remarkable that the computed r^{pop} values are lower than μ^* in the highly concentrated zones. It means that the amount of sugar assimilated will not be as important
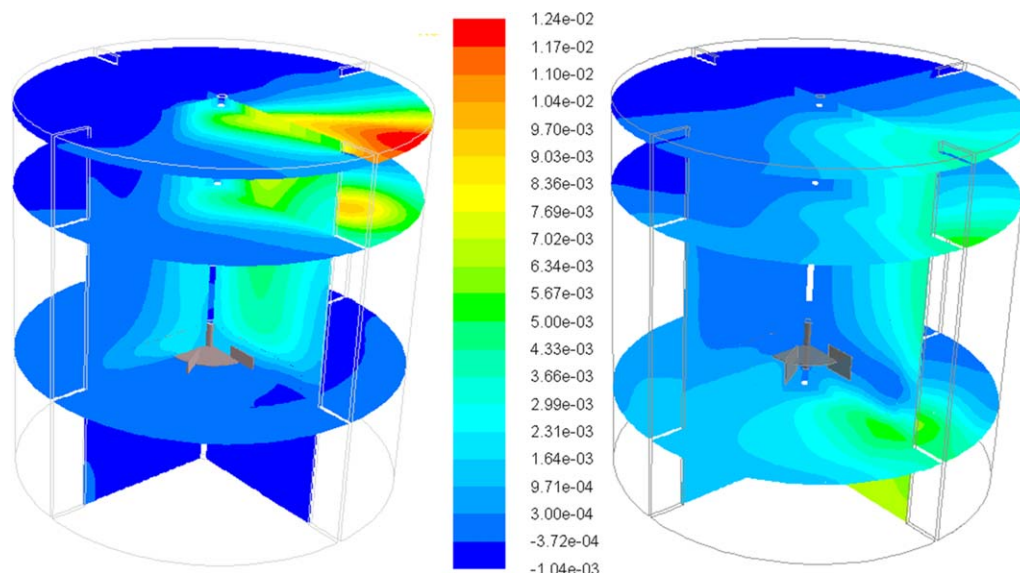
Figure 12. Contours of the difference r^{pop}-μ^{pop}: specific uptake rate minus population specific growth rate.

Top feed (left). Bottom feed (right). [Color figure can be viewed in the online issue, which is available at wileyonlinelibrary.com.]

as what is predicted when the local concentrations are used to compute the assimilation rate. This is quite interesting since it was pointed out that despite the use of CFD and metabolic model the substrate assimilation was generally over-estimated and the by-product formation under-estimated.[5,15] A possible explanation for this is that uptake and growth rates were calculated under the equilibrium assumption (from the local concentrations). In this context, the proposed population balance model that decouples the uptake rate from both the local concentrations and the specific growth rate constitutes a rational basis for the study of mixing issues in bioreactors. This shows that the proposition of the "out of equilibrium" concept makes sense here. In turn this works suggests that the limitation by the substrate may be considered as relative to the cell needs and not in an absolute way.

Conclusion

In this work, a development of CFD modeling including a population balance model for the biological phase has been successfully applied to 70 L and 70 m^3 fermentors. The scale-up, at fixed volumetric power draw, resulted in the formation of substrate and oxygen gradients at the largest scale due to the competition between mixing, transfer and reaction time scales. An unstructured kinetic model used with the CFD simulation furnishes quantitative data on what changes can be expected during the scale-up procedure. In the large-scale bioreactors, cells are exposed to concentration gradients which arise when the time scale of the reaction (typically substrate uptake) and the time scale of mixing are of the same order. The consequences of these gradients are investigated using a population balance model describing cell adaptation. Two dynamics corresponding to cell growth and substrate uptake were studied. It was found that growth, as a slow process, was essentially sensitive to the volume average concentrations whereas substrate assimilation, as a fast process, is more sensitive to the spatial distribution of the substrates. In any case, the biological phase is found to be "out of equilibrium" with the liquid phase, meaning that the biological rates are not algebraically linked to the local concentrations. This advanced modeling was used to analyze

and compare two bioreactors design. The local differences between the uptake rate and the growth rate induced by substrate concentration heterogeneities were used to quantify consequences of imperfect mixing on bioreactions.

Notation

a = interfacial area, m^{-1}
d_B = bubble diameter, m
D_l = liquid molecular diffusivity, m^2 s^{-1}
D_n = particle diffusivity, m^2 s^{-1}
k_l = liquid side mass transfer coefficient, m s^{-1}
k = turbulent kinetic energy, m^2 s^{-2}
k_la = mass transfer coefficient, s^{-1}
K_S = inhibition constant for the substrate, g L^{-1}
K_{O_2} = inhibition constant for the oxygen, g L^{-1}
N_p = power number
N = rotational speed, s^{-1}
O_2^* = local saturation concentration, g L^{-1}
P_g = gassed power input, W
P_0 = ungassed power input, W
$p_v(X)$ = volume of liquid at concentration X divided by the total volume
Q_g = gas flow rate, m^3 s^{-1}
r_S = reaction rate for substrate, g s^{-1} L^{-1}
r_{O_2} = reaction rate for oxygen, g s^{-1} L^{-1}
S = local substrate concentration (glucose), g L^{-1}
T = tank diameter, m
T_a = biological adaptation time constant
t_m = mixing time, s
t_{tr} = transfer time, s
t_S = reaction time (for the substrate), s
t_X = reaction time (for the biomass), s
u_R = local relative mean velocity, m s^{-1}
U_s = superficial velocity, m s^{-1}
V = tank volume, m^3
V_{inj} = Volume of the sugar injection zone, m^3
Y_{SX} = Yield coefficient, gram of S consumed by gram of X formed
X = cell concentration, g L^{-1}

Greek letters

α_g = gas volume fraction
ε = dissipation rate of the turbulent kinetic energy, m^2 s^{-3}
μ = local specific growth rate, s^{-1}
μ_∞ = macroscopic specific growth rate, s^{-1}
μ_{max} = maximum specific growth rate, s^{-1}
σ = surface tension, N m^{-1}

Literature Cited

1. Oosterhuis NMG, Groesbeek NM, Olivier APC, Kossen MWF. Scale down aspects of the gluconic acid fermentation. *Biotechnol Lett.* 1983;5(3):141–146.

2. Oosterhuis NMG, Kossen NWF. Dissolved oxygen concentration profiles in a production-scale bioreactor. *Biotechnol Bioeng.* 1984;26(5):546–550.

3. Larsson G, Tornkvist M, Wernersson ES, Tragardh C, Noorman H, Enfors SO. Substrate gradients in bioreactors: origin and consequences. *Bioprocess Biosyst Eng.* 1996;14(6):281–289.

4. George S, Larsson G, Olsson K, Enfors S-O. Comparison of the baker's yeast process performance in labototy an production scale. *Bioprocess Eng.* 1998;18:135–142.

5. Enfors SO, Jahic M, Rozkov A, Xu B, Hecker M, Jürgen B, Krüger E, Schweder T, Hamer G, O'Beirne D, Noisommit-Rizzi N, Reuss M, Boone L, Hewitt C, McFarlane C, Nienow A, Kovacs T, Trägårdh C, Fuchs L, Revstedt J, Friberg PC, Hjertager B, Blomsten G, Skogman H, Hjort S, Hoeks F, Lin HY, Neubauer P, van der Lans R, Luyben K, Vrabel P, Manelius Å. Physiological responses to mixing in large scale bioreactors. *J Biotechnol.* 2001;85(2):175–185.

6. Lara AR, Galindo E, Ramirez OT, Palomares LA. Living with heterogeneities in bioreactors. *Mol Biotechnol.* 2006;34(3):355–381.

7. Dunlop EH, Ye SJ. Micromixing in fermentors: metabolic changes in Saccharomyces cerevisiae and their relationship to fluid turbulence. *Biotechnol Bioeng.* 1990;36(8):854–864.

8. Wenger KS, Dunlop EH. 1994. Coupling of micromixing, macromixing and the glucose effect in continuous culture of Saccharomyces cerevisiae, in: AIChE Symposium Series. Industrial Mixing Technology: Chemical and Biological Applications. pp. 166–174.

9. Oosterhuis NMG, Kossen NWF, Olivier APC, Schenk ES. Scaledown and optimization studies of the gluconic acid fermentation by Gluconobacter oxydans. *Biotechnol Bioeng.* 1985;27(5):711–720.

10. Amanullah A, McFarlane CM, Emery AN, Nienow AW. Scale-down model to simulate spatial pH variations in large-scale bioreactors. *Biotechnol Bioeng.* 2001;73(5):390–399.

11. Neubauer P, Häggström L, Enfors SO. Influence of substrate oscillations on acetate formation and growth yield in Escherichia coli glucose limited fed-batch cultivations. *Biotechnol Bioeng.* 1995;47(2):139–146.

12. Lin YH, Neubauer P. Influence of controlled glucose oscillations on a fed-batch process of recombinant Escherichia coli. *J Biotechnol.* 2000;79(1):27–37.

13. Delvigne F, Destain J, Thonart P. Bioreactor hydrodynamic effect on Escherichia coli physiology: experimental results and stochastic simulations. *Bioprocess Biosyst Eng.* 2005;28(2):131–137.

14. Delvigne F, Lejeune A, Destain J, Thonart P. Modelling of the substrate heterogeneities experienced by a limited microbial population in scale-down and in large-scale bioreactors. *Chem Eng J.* 2006;120(3):157.

15. Schmalzriedt S, Jenne M, Mauch K, Reuss M. Integration of physiology and fluid dynamics. In: Advances in Biochemical Engineering/Biotechnology, Vol 80. Heidelberg: Springer Berlin, 2003:19–68.

16. Xu B, Jahic M, Enfors S-O. Modeling of overflow metabolism in batch and fed-batch cultures of "Escherichia coli." *Biotechnol Prog.* 1999;15(1):81–90.

17. Lin HY, Mathiszik B, Xu B, Enfors SO, Neubauer P. Determination of the maximum specific uptake capacities for glucose and oxygen in glucose-limited fed-batch cultivations of Escherichia coli. *Biotechnol Bioeng.* 2001;73(5):347–357.

18. Vrábel P, van der Lans RGJM, van der Schot FN, Luyben KCAM, Xu B, Enfors S-O. CMA: integration of fluid dynamics and microbial kinetics in modelling of large-scale fermentations. *Chem Eng J.* 2001;84(3):463–474.

19. Hristov H, Mann R, Lossev V, Vlaev SD, Seichter P. A 3-D analysis of gas-liquid mixing, mass transfer and bioreaction in a stirred bioreactor. *Food Bioproducts Process.* 2001;79(4):232.

20. Bezzo F, Macchietto S, Pantelides CC. Computational issues in hybrid multizonal/computational fluid dynamics models. *AIChE J.* 2005;51(4):1169–1177.

21. Lapin A, Muller D, Reuss M. Dynamic behavior of microbial populations in stirred bioreactors simulated with Euler-Lagrange methods: traveling along the lifelines of single cells. *Ind Eng Chem Res.* 2004;43(16):4647–4656.

22. Lapin A, Schmid J, Reuss M. Modeling the dynamics of E. coli populations in the three-dimensional turbulent field of a stirred-tank bioreactor–A structured-segregated approach. *Chem Eng Sci.* 2006;61(14):4783–4797.

23. Morchain J, Fonade C. A structured model for the simulation of bioreactors under transient conditions. *AIChE J.* 2009;55(11):2973–2984.

24. Morchain J, Gabelle J-C, Cockx A. Coupling of biokinetic and population balance models to account for biological heterogeneity in bioreactors. *AIChE J.* 2013;59(2):369–379.

25. Delafosse A, Line A, Morchain J, Guiraud P. LES and URANS simulations of hydrodynamics in mixing tank: comparison to PIV experiments. *Chem Eng Res Des.* 2008;86(12):1322–1330.

26. Delafosse A, Morchain J, Guiraud P, Liné A. Trailing vortices generated by a Rushton turbine: assessment of URANS and large Eddy simulations. *Chem Eng Res Des.* 2009;87(4):401–411.

27. Escudié R, Liné A. Experimental analysis of hydrodynamics in a radially agitated tank. *AIChE J.* 2003;49(3):585–603.

28. Escudié R, Liné A. A simplified procedure to identify trailing vortices generated by a Rushton turbine. *AIChE J.* 2007;53(2):523–526.

29. Kerdouss F, Bannari A, Proulx P. CFD modeling of gas dispersion and bubble size in a double turbine stirred tank. *Chem Eng Sci.* 2006;61(10):3313–3322.

30. Scargiali F, D'Orazio A, Grisafi F, Brucato A. Modelling and simulation of gas-liquid hydrodynamics in mechanically stirred tanks. *Chem Eng Res Des.* 2007;85(5):637–646.

31. Harnby N, Edwards MF, Nienow AW. Mixing in the Process Industries. Academic press, London, 1985.

32. Nienow AW. Agitators for mycelial fermentations. *Trends Biotechnol.* 1990;8:224–233.

33. Ranade VV. Computational Flow Modeling for Chemical Reactor Engineering. Academic Press: New York, 2002.

34. Talvy S, Cockx A, Liné A. Modeling of oxygen mass transfer in a gas-liquid airlift reactor. *AIChE J.* 2007;53(2):316–326.

35. Talvy S, Cockx A, Liné A. Modeling hydrodynamics of gas-liquid airlift reactor. *AIChE J.* 2007;53(2):335–353.

36. Fayolle Y, Cockx A, Gillot S, Roustan M, Héduit A. Oxygen transfer prediction in aeration tanks using CFD. *Chem Eng Sci.* 2007;62(24):7163.

37. Garnier C, Lance M, Marié J. Measurement of local flow characteristics in buoyancy-driven bubbly flow at high void fraction. *Exp Therm Fluid Sci.* 2002;26(6–7):811–815.

38. Colombet D, Legendre D, Cockx A, Guiraud P, Risso F, Daniel C, Galinat S. Experimental study of mass transfer in a dense bubble swarm. *Chem Eng Sci.* 2011;66(14):3432–3440.

39. Simonin O, Viollet PL. Modeling of turbulent two-phase jets loaded with discrete particles. In: Phase-Interface Phenomena in Multiphase Flows. Hemisphere Publishing Corp., Washington DC, 1990:259–269.

40. Lamont JC, Scott DS. An eddy cell model of mass transfer into the surface of a turbulent liquid. *AIChE J.* 1970;16(4):513–519.

41. Linkès M, Martins Afonso M, Fede P, Morchain J, Schmitz P. Numerical study of substrate assimilation by a microorganism exposed to fluctuating concentration. *Chem Eng Sci.* 2012;81:8–19.

42. Ramkrishna D. Population Balances: Theory and Applications to Particulate Systems in Engineering. Academic Press, San Diego CA, 2000.

43. Augier F, Morchain J, Guiraud P, Masbernat O. Volume fraction gradient-induced flow patterns in a two-liquid phase mixing layer. *Chem Eng Sci.* 2003;58(17):3985–3993.

44. Van't Riet K, Tramper J. Basic Bioreactor Design, CRC Press. 1991.

45. Gabelle J-C, Augier F, Carvalho A, Rousset R, Morchain J. Effect of tank size on kLa and mixing time in aerated stirred reactors with non-newtonian fluids. *Can J Chem Eng.* 2011;89(5):1139–1153.

46. Whitton MJ, Nienow AW. Scale up correlations for gas holdup and mass transfer coefficients in stirred tank reactors. In: Proceeding of 3rd International Conference on Bioreactor and Bioprocess Fluid Dynamics. London: BHR Group/Mep, 1993:135–149.

47. Gabelle J-C. 2012. Analyse locale et globale de l'hydrodynamique et du transfert de matière dans des fluides à rhéologie complexe caractéristiques des milieux de fermentation (PhD Thesis). INSA Toulouse.

48. Bombač A, Žun I, Filipič B, Žumer M. Gas-filled cavity structures and local void fraction distribution in aerated stirred vessel. *AIChE J.* 1997;43(11):2921–2931.

49. Baldyga J, Bourne JR. Turbulent Mixing and Chemical Reactions. Chichester: Wiley, 2003.

50. Chassagnole C, Noisommit-Rizzi N, Schmid JW, Mauch K, Reuss M. Dynamic modeling of the central carbon metabolism of Escherichia coli. *Biotechnol Bioeng*. 2002;79(1):53–73.

51. Natarajan A, Srienc F. Glucose uptake rates of single E. coli cells grown in glucose-limited chemostat cultures. *J Microbiol Methods*. 2000;42(1):87–96.

52. Leegwater MPM, Neijssel OM, Tempest DW. Aspects of microbial physiology in relation to process control. *J Chem Technol Biotechnol*. 1982;32(1):92–99.

53. Lin YH, Neubauer P. Influence of controlled glucose oscillations on a fed-batch process of recombinant Escherichia coli. *J Biotechnol*. 2000;79(1):27–37.

54. Lendenmann U, Egli T. Kinetic models for the growth of Escherichia coli with mixtures of sugars under carbon-limited conditions. *Biotechnol Bioeng*. 1998;59(1):99–107.

55. Namdev PK, Thompson BG, Gray MR. Effect of feed zone in fed-batch fermentations of Saccharomyces cerevisiae. *Biotechnol Bioeng*. 1992;40(2):235–246.

Appendix

Convergence

Judging convergence is particularly difficult in this type of CFD simulation consisting of coupled momentum, mass transfer and reaction equations in a closed vessel. Beyond the numerical criterion, a suitable way to assess the quality of the simulation is to check mass balances manually. In this work, the check was carried out by writing an additional User Defined Subroutine in Fluent®. The volume integral of local mass transfer and local reaction terms were computed. These integrals were further compared to the global mass balance at the reactor scale. As for the substrate, the integral of the source term is compared to the integral of the sink term due to the biological reaction in the liquid phase.

$$\iiint_V \rho Q_V(S) dv = \iiint_V r_S dv \qquad (A1)$$

Because of the stoichiometry of the biological reaction, one gram of oxygen consumed par gram of substrate, the coupling between reaction and gas-liquid mass transfer is also verified by checking that the mass flux of oxygen transferred to the liquid, $T(O_2)$, equals the amount of substrate, $R(S)$, consumed by the reaction per unit of time

$$\underbrace{\iiint_V r_S dv}_{R(S)} = \underbrace{\iiint_V kl.\frac{6\varepsilon_G}{d_B}.(m.O_{2,gas} - O_{2,liq}) dv}_{T(O_2)} \qquad (A2)$$

Assessing the simulations

It was explained that the operating conditions are such that substrate concentration gradients will be present in the large scale bioreactor. It is interesting to build global variables which can possibly reflect the consequences at the reactor scale:

- macroscopic specific growth rate, μ_∞, computed from the mass balance on the substrate assuming perfect mixing, homogeneous gas dispersion and no oxygen limitation (see Eq. 18 for the definition)
- growth rate, μ, based on the volume average concentrations (noted $<\,>$)

$$\mu = \mu_{max} \frac{\langle S \rangle}{K_S + \langle S \rangle} . \frac{\langle O_{2,liq} \rangle}{K_{O_2} + \langle O_{2,liq} \rangle} = \mu_{max} \Gamma(\langle S \rangle).\Gamma(\langle O_{2,liq} \rangle)$$

$$(A3)$$

It is also interesting to average local variables to reflect the integral consequences at the reactor scale

- $<\mu^*>$: volume average of the local specific growth rates

$$\langle \mu* \rangle = \left\langle \mu_{max} \frac{S}{K_S + S} . \frac{O_{2,liq}}{K_{O_2} + O_{2,liq}} \right\rangle = \mu_{max} \langle \Gamma(S).\Gamma(O_{2,liq}) \rangle \quad (A4)$$

- $<\mu^{pop}>$: volume average of the local population specific growth rate as defined in Eq. 21. This value reflects the two-way coupling and appears in bold in Table 5

In the case of a perfectly mixed reactor, $<\mu^*>$ and μ are equal. If the gas hold-up is also homogeneous, one have $\mu_\infty = <\mu^*>$ since le local gas hold-up has no longer any effect on the volume averaging. In any other situation, with imperfect mixing and/or heterogeneous gas phase distribution, $<\mu^*>$, μ, μ_∞ should be different. This is due to the nonlinearity of the relationship between the specific growth rate and the substrates concentrations.